Micro-Precision Interferometer: Pointing control system performance in on-orbit disturbance environment.

Frank G. Dekens, Greg Neat

Jet Propulsion Laboratory 4800 Oak Grove Drive Pasadena, CA 91109

ABSTRACT

We investigate how the Space Interferometer Mission (SIM) will be able to meet its instrument astrometric pointing requirements. The most demanding SIM pointing requirement is to independently point each interferometer arm to better than 0.14 micro-radian RMS residual jitter using a 0.01 Hz bandwidth sensor. The predominant contributors to the pointing error are the spinning spacecraft reaction wheel assemblies. An estimate of the residual pointing error is presented, for cases where the reaction wheels assemblies are hard-mounted or isolated. Central to this estimate is the Micro-Precision Interferometer (MPI) testbed which is a softly suspended hardware model of a future space-borne optical interferometer and is dimensionally representative of SIM. The prediction of the on-orbit pointing error is determined by measuring broadband disturbance transfer functions from the testbed's isolated reaction wheel location to the camera output, where the pointing must be stabilized. In order to predict the residual pointing error over the entire range of wheel speeds, for a set of four wheels, an off-line procedure combines the measured testbed transfer functions with an empirical model of the reaction wheel disturbance. Results suggest that the most demanding SIM pointing requirement is violated by a factor of three.

Keywords: space interferometry, isolation system, interferometry testbed, pointing control

1. INTRODUCTION

Optical interferometers use an array of two or more small telescopes, as opposed to a single large telescope, to collect light from a single target star. The light from these telescopes, or sub-apertures, is combined to create an interference fringe pattern. Space Interferometer Mission (SIM) is a first-generation space-borne interferometer concept with astrometric and imaging goals.[1] The instrument will provide milli-arcsec imaging capabilities, micro-arcsec astrometric measurement capabilities and a technology demonstration of the nulling function. To achieve these goals, the cumulative displacements of the optical elements must be at the nanometer level and the beam pointing stability must be at the nano-radian level. Unlike ground-based interferometers bolted to bedrock,[?] instrument optics of SIM will be distributed across a 10 m, light-weight flexible structure. In the presence of the primary mechanical disturbance source, the spinning reaction wheels, simulation results suggest that in the unattenuated spacecraft environment these stability requirements would be violated by as much as a factor of 1000.[2] This discrepancy inspired a layered vibration attenuation control strategy which involves the blending of vibration isolation, structural quieting, and active optical control. Evaluating such a strategy in a ground test environment implies an additional challenge of accurately representing the on-orbit disturbance conditions. To date, a number of testbeds have been designed, built and exercised to evaluate the progress on meeting the displacement or optical path-length difference requirement. We now addresses the status of meeting the pointing requirements.

Central to assessing pointing performance is the Micro-Precision Interferometer (MPI) testbed .[3,4] Fig. 1 shows a bird's eye view of the MPI testbed. Located at the Jet Propulsion Laboratory, the testbed contains all the subsystems necessary to assess the effectiveness of the vibration attenuation technologies. These subsystems are: a 7 m x 7 m x 6.5 m softly suspended truss structure with mounting plates for subsystem hardware; a six-axis vibration isolation system which can support a reaction wheel assembly to provide a flight-like input disturbance source; a complete Michelson interferometer; internal and external metrology systems; and a star simulator that provides stellar-like input to the interferometer collecting apertures.

Further author information: (Send correspondence to F.G.D.)
F.G.D.: E-mail: fdekens@jpl.nasa.gov
G.N.: E-mail: neat@huey.jpl.nasa.gov

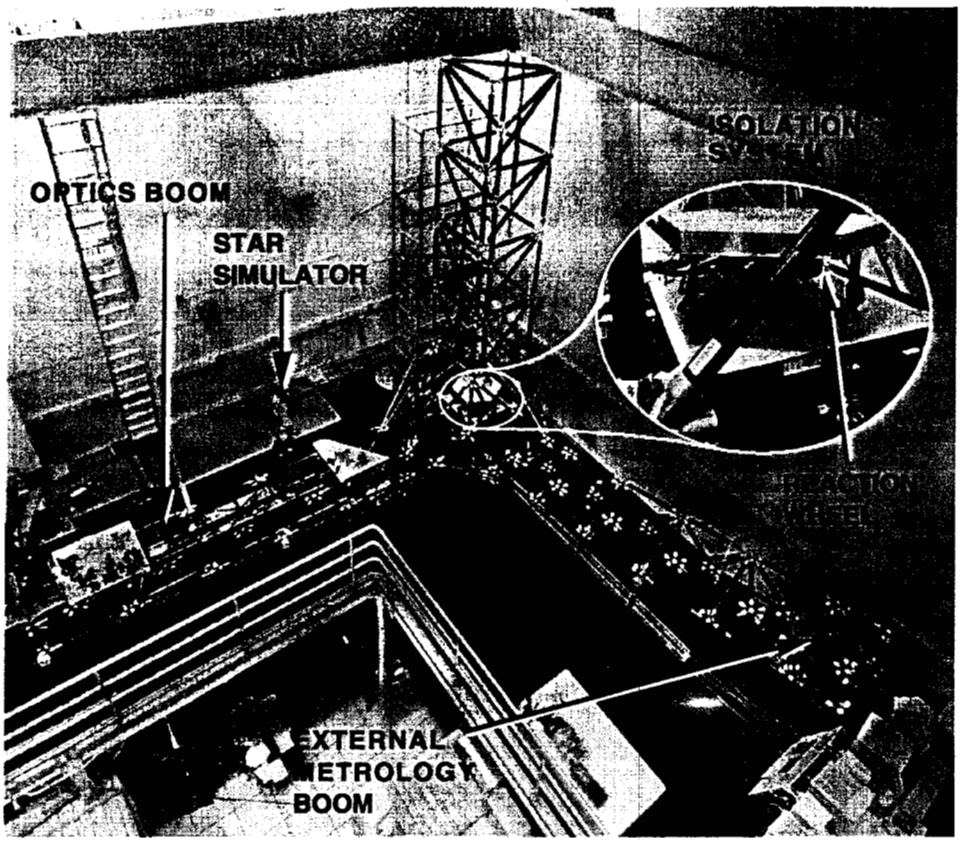

Figure 1. Bird's eye view of the MPI testbed with inset showing a close-up of a six-axis isolation system.

Previous MPI studies [?,?] have assessed the severity of the on-orbit optical path difference (OPD) problem using an on-orbit prediction algorithm. The performance prediction procedure involves measuring disturbance transfer functions in six degrees of freedom from the reaction wheel attachment location to the output optical sensor. These transfer functions accurately depict (in a linear sense) how the disturbance propagates from the source to the optical detector. Modeled reaction wheel disturbance profiles are then played through this family of measurements to predict the on-orbit performance in terms of the desired optical metric. This same procedure is now used to predict the pointing error, as measured by a CCD camera, as a function of wheel speed rather than optical path difference as a function of wheel speed.

We focus on the most challenging pointing problem, which is pointing the "science" interferometer. Each arm of this interferometer must be stabilized to 14 nano-radians RMS while using a .01 Hz bandwidth sensor, which is effectively open loop. The only vibration attenuation strategy which can fight the reaction wheel disturbance at higher frequencies is the reaction wheel vibration isolation system. In addition to the open loop optics, isolated reaction wheel configuration, two other tests were performed to understand limitations of our measurement setup. One was a hard mounted, open loop optic configuration which represents the maximum signal possible. The other case is the "perfect" isolator configuration, in which the disturbance is detached from the structure, and the pointing loop is closed using a fast steering mirror (FSM). This measurement provides the lower bound on our measurement or equivalently tells us the noise floor

Sec. 2 presents the fundamentals of the pointing system for an interferometer and describes the specific MPI pointing system. In Sec. 3, we discuss how the MPI pointing problem relates to the SIM pointing problem. The product of this section is a pointing requirement which must be satisfied by the MPI system in order to prove the SIM system will meet its corresponding requirement.

The on-orbit prediction approach is described in Sec. 4. In Sec. 5We discuss how the data is collected and processed to predict the on-orbit pointing performance for different testbed configurations. In Sec. 6 we discuss the

three different test configurations and present the results from each. Finally, we compare the performance predictions with the derived requirements to determine the status of the pointing problem.

2. POINTING SYSTEM DESCRIPTION

We will first briefly describe the MPI testbed. Fig. 2 is a schematic of the MPI optics boom and traces the optical path from the artificial star through the testbed's optical train. The artificial star is a commercial heterodyne laser

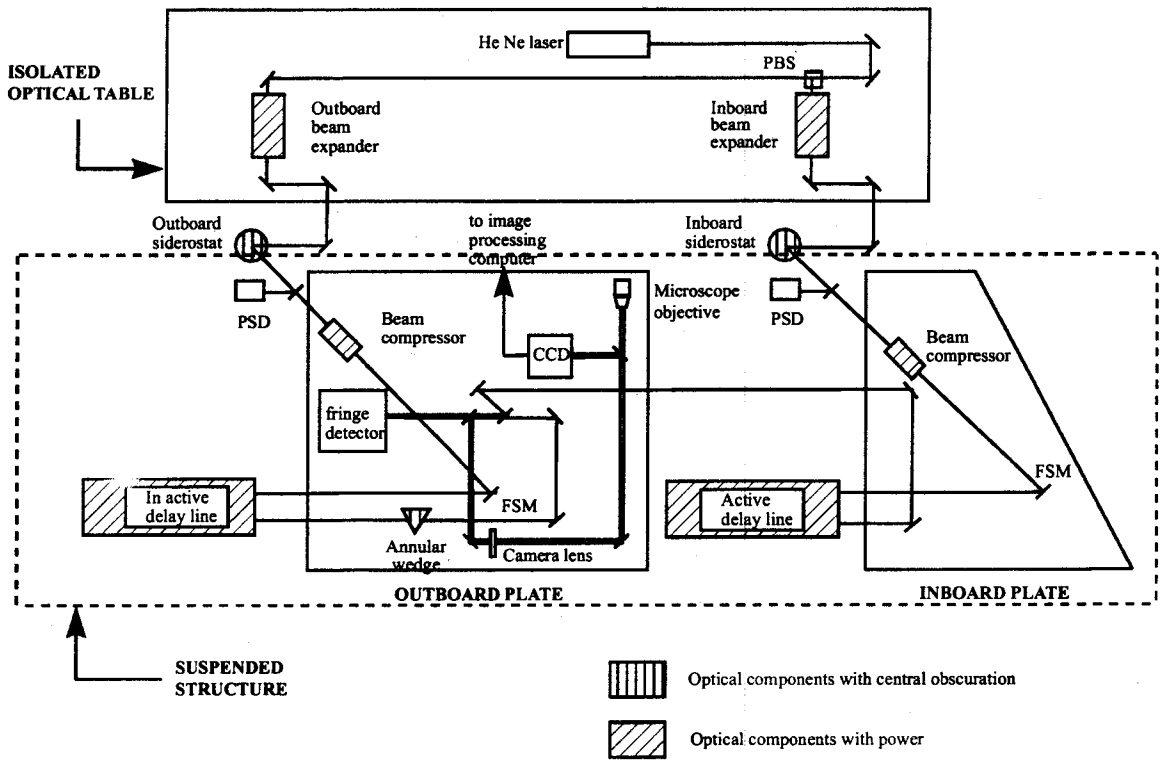

Figure 2. Optical layout of the Micro-Precision Interferometer.

that sits on a pneumatically supported optical table. The beam is split by a polarizing beam-splitter (PBS) and each side is expanded to a 5 cm beam. A number of fold mirrors direct the beams to the two interferometer arms on the suspended MPI structure. The light path taken by the right-hand beam is described below, and the other path is similar. For the purposes of this paper, we only consider the right-hand side and will therefor describe its path. The left-hand path was blocked for all measurements described in this paper. The siderostat is the first optical element on the air suspended structure. A subsequent beam compressor is used to reduce the input beam diameter from 5 cm to 3 cm to obtain an output beam suitable for traversing the delay line optics with sufficient light for the fringe-tracking sensor. Next comes a fast steering mirror (FSM) which is used for pointing control. Three piezo actuators position the mirror, providing tip and tilt motion for the closed-loop configuration, without introducing path length changes. After traveling through the active delay-line and a couple of folding mirrors, the inboard beam is reflected on a 50% beam splitter. Here the reflected light would join the transmitted beam from the left-handed path. After the beam combiner, the central portion of the combined stellar beams passes through the hole in an annular pick-off mirror to a fringe detector. The annular pick off mirror and subsequent folding mirrors reflects the outer annulus of each beam towards a high speed CCD camera. The 32 by 32 pixel CCD camera is the sensor for the pointing control subsystem. The beam is focused, by a 1 meter focal length lens, to a location on the CCD camera. A 5 by 5 pixel window is sampled at 4000 Hz, centered on the diffraction pattern location. The first moment of the diffraction pattern is calculated, which we refer to as the centroid location. This is calculated as follows. Let I(i,j) be the intensity of the $(i,j)^{th}$ pixel in the CCD window. The offset from the center pixel is

$$\Delta x = \frac{\sum_{j=-isize}^{isize} \sum_{i=-isize}^{isize} iI(i+i_c, j+j_c)}{\sum_{j=-isize}^{isize} \sum_{i=-isize}^{isize} I(i+i_c, j+j_c)} \quad (1)$$

where $isize$ is 2 in this case and (i_c, j_c) is the center pixel determined when the measurement is first begun by the brightest pixel. Thus first image is used as a reference. The centroiding box is not moved. If a centroid moves outside of the range of the box during a measurement, the measurement is repeated. For subsequent frames, the offset from of the current centroid location to the reference centroid location is converted to two analog signals (the x and y offsets on the CCD coordinate system). The centroiding calculation is done in real time, at 4000 Hz, and the offsets are used as the output to a signal analyzer.

3. MAPPING MPI TO SIM

The current space interferometer design is planned to be on a 10 meter long flexible truss structure. The relevant baseline design parameters are shown in Table 1 along with the MPI requirements. The pointing requirements for MPI

	SIM	MPI
Beam diameter	33 cm	3 cm
Compressor	11:1	1:1.5
Wavefront tilt requirement	80 nrad	—
Maximum jitter on the detector	880 nrad	80 nrad

Table 1. SIM vs. MPI.

are such that if they are met, we have confidence that SIM will be able to obtain its pointing requirement on-orbit. The argument that MPI needs to meet the wave-front tilt requirements at the detector, despite the different optics and SIM's relaxed wave-front tilt requirements at the detector, goes as follows. (For the purposes of this discussion, we assume there are only tip/tilt errors.) What drives the requirement, is that the RMS tilt error between the two wavefronts from the different paths of the interferometer be less than 80 nrad at the largest aperture size of 33 cm. Referring to Fig. 3, suppose that all optics on SIM are stationary, except for the siderostat of one arm, which is tilting by 80 nrad RMS. As the light passes through the beam compressor, this angle in increased to 880 nrad at the 3 cm aperture. This means that SIM, at the detector, only needs to control or have less than 880 nrad RMS tilt error. If instead of the siderostat a different optic is moving, which is past the compressor, it may move up to 880 nrad and still meet the required RMS tilt error because now the diameter has decrease by a factor of 11. This means that, at the detector, SIM may see 11 times the required jitter which is due to the compressor and the most critical optical element is the siderostat, which is the only optical element that needs to be stationary (or compensated for) to 80 nrad. On MPI however, we do not have such a compressor (we will ignore the small compression ratio of 1:1.5 for this discussion). In order to guarantee that the siderostat does not move by more than 80 nrad, we need to stabilize the complete path to this level, since we can not distinguish which optics are moving. Thus MPI needs to have the wavefront tilt requirement of SIM at the MPI detector, not the wavefront at the SIM detector. MPI is therefore solving a slightly more difficult problem, in that MPI requires the combination of all the optics jitters to be less than 80 nrad, whereas SIM only needs the siderostat to be that stable. Care will have to be taken for the SIM sensor requirements, such that it can detect the centroid motion which is allowed to be 10 times larger, and the FSM will need to be able to control the larger motion. Note that neither of these are technical problems, just design considerations.

We have assumed that SIM will have a final beam size of 3 cm which is used for the angle measurement (similar to the MPI beam size), and that the F ratio and camera pixel size will be similar. Although we anticipate better reading noise in the camera used by SIM, we do not attempted to correct for this, which is being more conservative.

4. PERFORMANCE PREDICTION PROCEDURE

The performance evaluation procedure combines disturbance transfer function measurements from the testbed with an analytical disturbance model, in order to assess pointing system performance over the entire range of disturbance conditions expected on-orbit during instrument observations. This hybrid experimental/analytical procedure predicts on-orbit performance in an accurate, efficient manner. Measuring performance solely in hardware would require measuring the optical metric while stepping through all combinations of wheel speeds for the four reaction wheel assemblies. The time required to perform this measurement is prohibitive. The test would also require having at

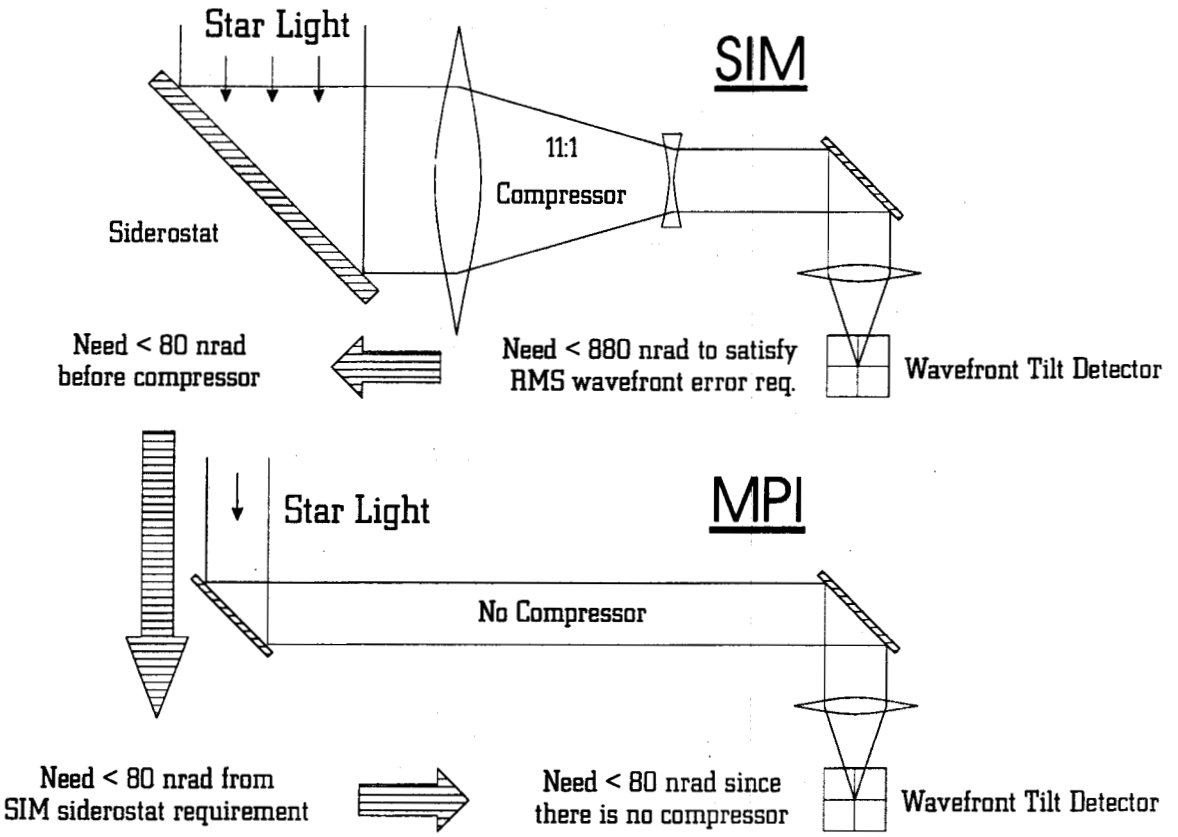

Figure 3. Comparison of optics and requirement of MPI verses SIM.

least one reaction wheel and a suspension system to stabilize the testbed attitude in the presence of the spinning wheel. In addition, the time domain optical sensor data would be corrupted with ambient disturbances not traceable to space such as rigid body motion of the suspended structure, pseudo star motion, atmospheric effects on the laser beams, and acoustic disturbances from the ambient lab environment. Conversely, performing this assessment solely in analysis would require an accurate analytical representation (over all frequencies) of the structure, control system sensors and actuators and the disturbance sources. Attaining the necessary model fidelity is a challenge; especially at higher frequencies ($> 100Hz$).[5] In addition, it is difficult to accurately represent the actuators and sensors, particularly with respect to practical implementation constraints such as noise floors and dynamic ranges.

Fig. 4 shows how the task of accurately representing the on-orbit problem has been distributed between the hardware and analysis tools. The four steps which make up this procedure are: (1) the analytical reaction wheel disturbance model, (2) measuring disturbance transfer functions, (3) the performance prediction algorithm yielding the predicted RMS jitter as a function of wheel speed for each of the tips and tilts for the two arms of the interferometer, and (4) combining it all to a set of metrics which accurately predict the on-orbit jitter performance. Each of these steps is described in the following four sub-sections.

4.1. Reaction Wheel Model

Based on test data obtained from a HST flight reaction wheels,[?] the disturbance forces and torques are modeled as discrete harmonics of the reaction wheel speed, f_{rwa}, with amplitudes proportional to the wheel speed squared:

$$m(t) = \sum_{i=1}^{n} C_i f_{rwa}^2 \sin\left(2\pi h_i f_{rwa} t + \phi_i\right) \tag{2}$$

where $m(t)$ is the disturbance torque or force, C_i is an amplitude coefficient, h_i is the harmonic number, and ϕ_i is a random phase (uniform over $[0,\ 2\pi]$) used to account for phase uncertainty. According to this model, h_i and C_i

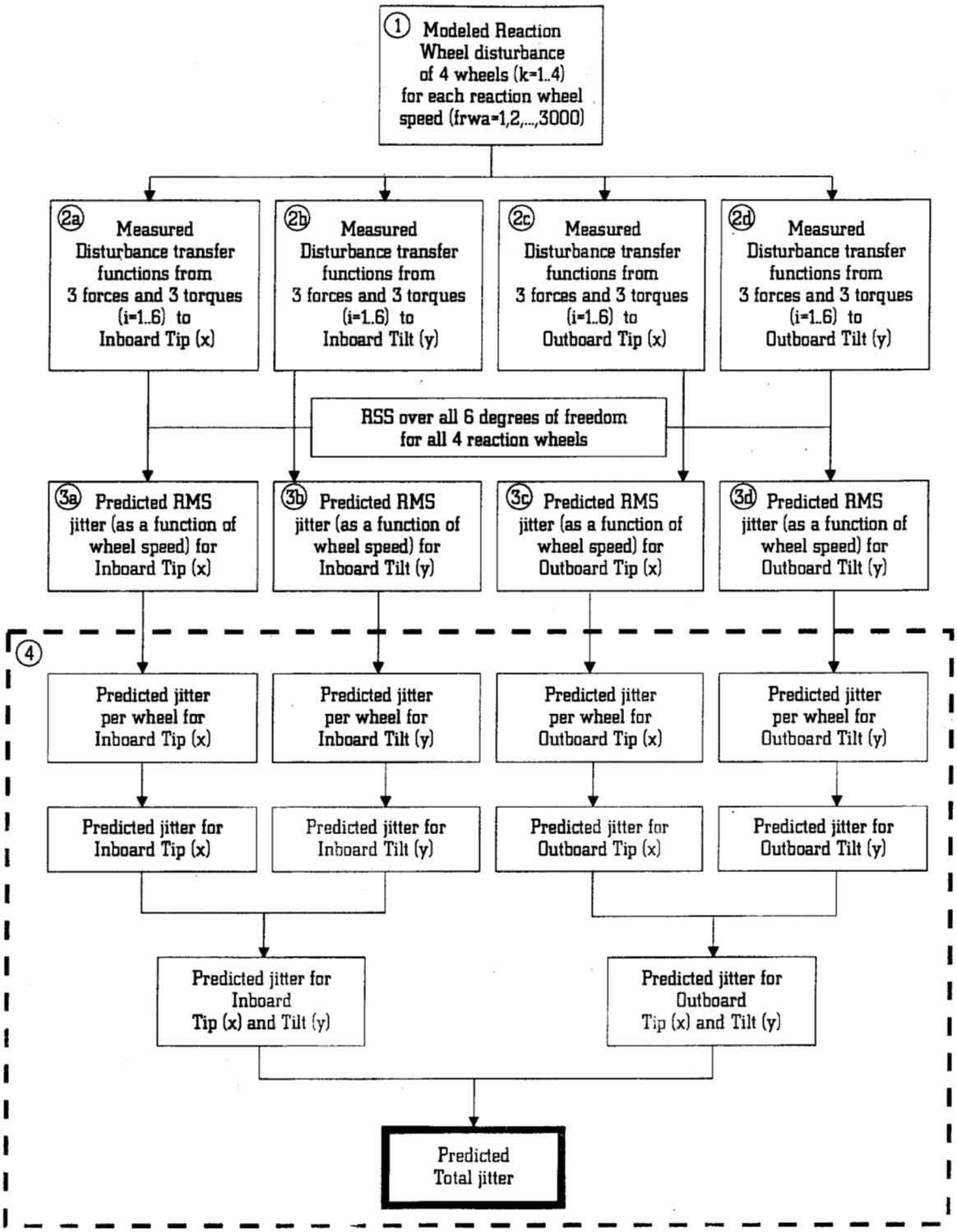

Figure 4. Data process to obtain on-orbit residual RMS tip/tilt error prediction.

uniquely determine the amplitude and frequency of each harmonic component for a given wheel speed. Melody et. al.[6] give the values for the different harmonics.

The disturbance model include one axial force (about the wheel spin axis), two radial forces (normal to the spin axis), and two radial torques (causing wheel wobble). These disturbances result from wheel imbalances and bearing

imperfections.[?] Disturbance torque about the axis of rotation (from torque ripple or motor clogging) was found to be insignificant, and is therefor omitted.

The procedure requires reaction wheel disturbance power spectral densities as input to the measured transfer functions. Given that the reaction wheel disturbances are sinusoidal wheel harmonics (Eq. 2), and assuming that the random phases (ϕ_i) are independent, identically-distributed,[7] the power spectral densities consist of Dirac delta functions[?] at the harmonic frequencies:

$$\Phi_m(\omega) = \sum_{i=1}^{n} \frac{\pi C_i^2 f_{rwa}^4}{4} \left[\delta\left(\omega - 2\pi h_i f_{rwa}\right) + \delta\left(\omega + 2\pi h_i f_{rwa}\right)\right] \tag{3}$$

where $\Phi_m(\omega)$ is the power spectral density of $m(t)$, and $\delta(t)$ is the Dirac delta function. As an example, Fig. 5 shows the power spectral density of axial force at a wheel speed of 1500 RPM.

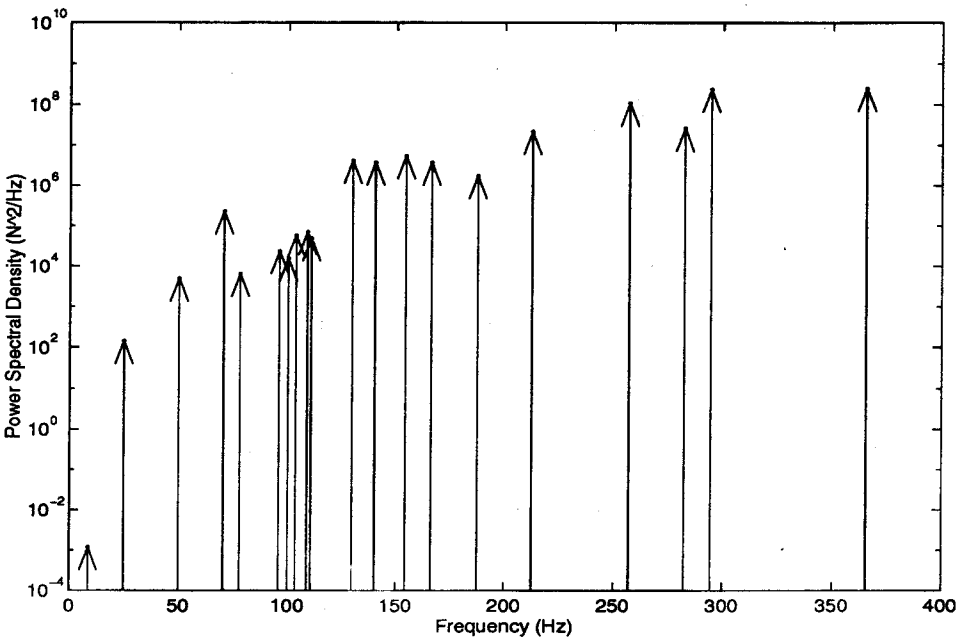

Figure 5. HST reaction wheel axial force disturbance PSD for a wheel spinning at 1500 RPM (Dirac delta function peaks are represented as arrows).

4.2. Disturbance Transfer Function Measurements

The disturbance source consists of a pair of shakers mounted to a custom six-axis force measuring device (dynamometer). The dynamometer is mounted on the payload structure and measures the forces and torques transmitted to the payload structure. Fig. 6 shows the dynamometer with the two shakers. The dynamometer is a six degrees of freedom disturbance sensor. These six outputs are the three forces (X, Y and Z directions) and the three torques (along the X, Y and Z axis). The mechanical parts consist of the base plate, 6 load cells, 12 flexures and the top plate. The top plate is mounted to the base of the dynamometer only through the six load cells, three in the vertical direction a. d three in the horizontal one. The load cells are arranged in a triangular configuration. Two flexures are mounted on each side of the load cell to reduce the coupling between load cells. These flexures have to be soft enough the reduce the coupling but stiff enough so that the dynamometer modes are located above the frequency range of interest ($> 750Hz$).

Signal conditioning parts consist of the load cell signal amplifier and the analog transformation matrix board. This board converts the six signals from the six load cells into six outputs (X, Y, Z forces and X, Y, Z torques).

An HP signal analyzer is used to measure disturbance transfer functions. The HP unit generates a broadband drive signal. This signal is sent to the two shakers through two power voltage amplifiers. To generate torques,

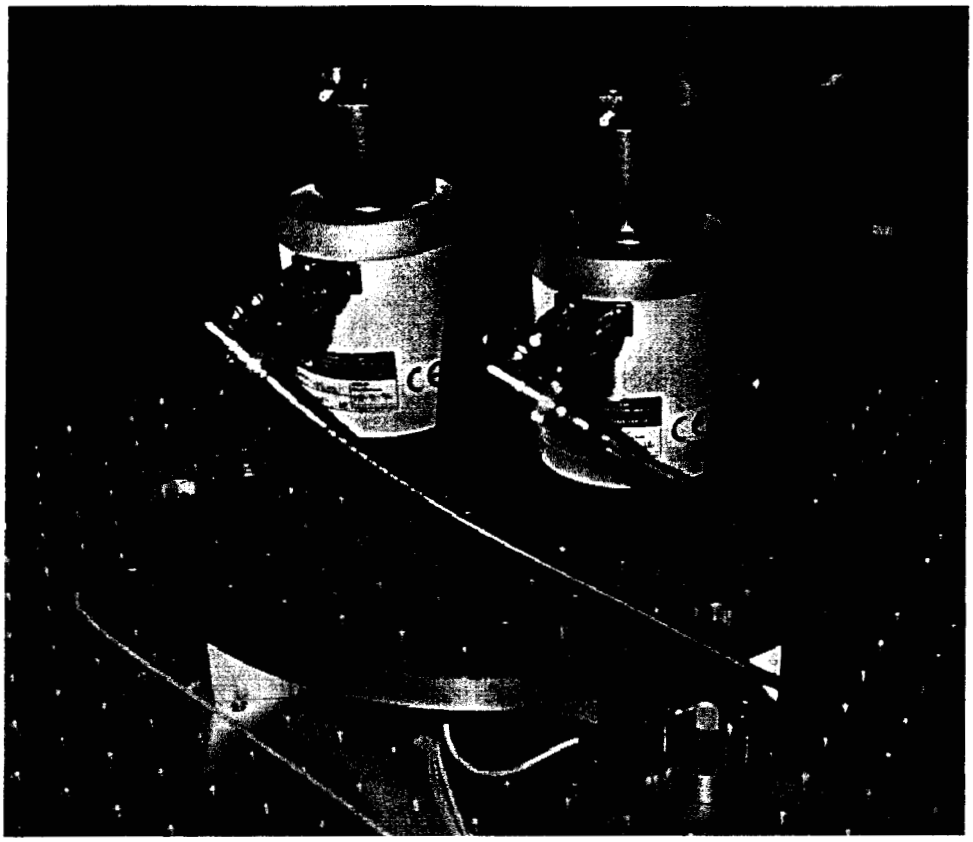

Figure 6. Dynamometer with two linear shakers on top producing a Z force shown on an optics bench. A load-cell between two flexure can be seen on the lower right of the picture.

polarity is inverted on one of the shakers. The bandwidth is divided into 3 ranges (2 - 14.5 Hz, 10 - 110 Hz and 100 - 900 Hz) with the driving voltage increasing with the frequency.

The dynamometer signal conditioner produces a voltage proportional to the disturbance. This voltage is sent to the HP analyzer as the input for the transfer function. The shakers are manually re-oriented to measure the six different transfer functions. The output for the transfer function is the tip/tilt offset, which was described in Sec. 2.

4.3. Performance Prediction Algorithm

In the analysis, the on-orbit disturbance environment consists of four wheels, as SIM is expected to carry a fourth RWA for redundancy. These wheels were assumed to be in a pyramidal configuration, i.e., the axis of each wheel is normal to a side of a square pyramid. The angle of the pyramid was assumed to be 63°, since this yielded equal torque capacity in all three spacecraft axes. Associated with each wheel orientation is a set of RWA local coordinates and a transformation from local to global coordinates. Applying this transformation to the disturbance transfer functions yielded transfer functions from each RWA local disturbance direction to the inboard and outboard wave front tip or tilt for each RWA. That is, from the twenty four global transfer functions $H_n(\omega)$, eighty local transfer functions, $\tilde{H}_{jk}(\omega)$, were created (five disturbance directions per wheel times four wheels for both tip and tilt on both the inboard and outboard arms). These eighty transfer functions were then the input to the disturbance model algorithm in order to determine wave front tip or tilt as a function of wheel speed.

The algorithm contains two nested loops with the outer loop indexing each wheel orientation (k=1-4) while the inner loop steps through all possible wheel speeds ($[f_{rwa}]_i$ = 1-3000 RPM). The kernel of the algorithm is the calculation of a wave front tip or tilt standard deviation, $[\sigma_{tip}]_{ik}$, for a single wheel speed (i-index) and orientation (k-index). For each wheel orientation, this calculation begins with five RWA disturbance PSDs generated from the wheel speed, f_{rwa} (an example RWA disturbance PSD is shown in Fig. 5). These PSDs, $[\Phi_m]_{ji}(\omega)$, are multiplied by

the modulus squared of their corresponding local disturbance transfer functions, $\tilde{H}_{jk}(\omega)$, and summed to yield the wave front tip or tilt PSD, $[\Phi_{fp}]_{ik}(\omega)$:

$$[\Phi_{tip}]_{ik}(\omega) = \sum_{j=1}^{5} \left|\tilde{H}_{jk}(\omega)\right|^2 [\Phi_m]_{ji}(\omega) \tag{4}$$

The cumulative area under the wave front tip PSD, $\left[\sigma^2_{tip}\right]_{ik}(\omega)$, is calculated by integrating the PSD, $[\Phi_{tip}]_{ik}(\omega)$, over $[0,\omega]$:

$$\left[\sigma^2_{tip}\right]_{ik}(\omega) = \int_0^{\omega} \frac{1}{\pi} [\Phi_{tip}]_{ik}(\tilde{\omega})\, d(\tilde{\omega}) \tag{5}$$

When the integration limit approaches infinity, the cumulative PSD equals the variance, $\left[\sigma^2_{tip}\right]_{ik}$. The square root of this variance is the tip/tilt standard deviation, $[\sigma_{tip}]_{ik}$, for a given wheel speed and orientation. This value ($[\sigma_{tip}]_{ik}$) represents a single point in the plot of tip/tilt jitter as a function of wheel speed (RPM). This procedure produces four plots of σ_{tip} vs. f_{rwa}, one for each of the four wheel orientations. For a given plot, each point represents the standard deviation of a discrete-frequency power spectral density. It is not meaningful to combine these four plots into a single plot of σ_{tip} vs. a single wheel speed, since the four wheel speeds are generally not equal.

4.4. Metrics

The methodology uses two metrics for overall the pointing jitter performance: one which represents nominal operating conditions and one which represents worst case operating conditions. For each wheel, the worst-case metric, $[\sigma_{\max}]_k$, is the maximum $[\sigma_{tip}]_k(f_{rwa})$ over the range of wheel speeds. The nominal metric, $[\sigma_{rss}]_k$, is the root-sum-square of $[\sigma_{tip}]_k(f_{rwa})$ over the wheel speed (i.e., the square root of the average variance)*. Both $[\sigma_{rss}]_k$ and $[\sigma_{\max}]_k$ for each of the four wheel orientations are root-sum-squared to assess the residual jitter of all four reaction wheels. This still produces four sets of metrics, tip and tilt for both the inboard and outboard side. Finally, we assume that all four of these degrees of freedom are uncorrelated. We therefore take the room-sum-square of all four values to produce the final single nominal and maximum predicted jitter performance.

5. TEST CONFIGURATIONS

In all configurations, the shakers and dynamometer are mounted to a triangular payload plate. This presents our disturbance source. There are three different methods in which this is mounted to the testbed, as shown in Fig. 7. First is the hard-mounted case, where the disturbance source is mounted through three metallic posts to the base

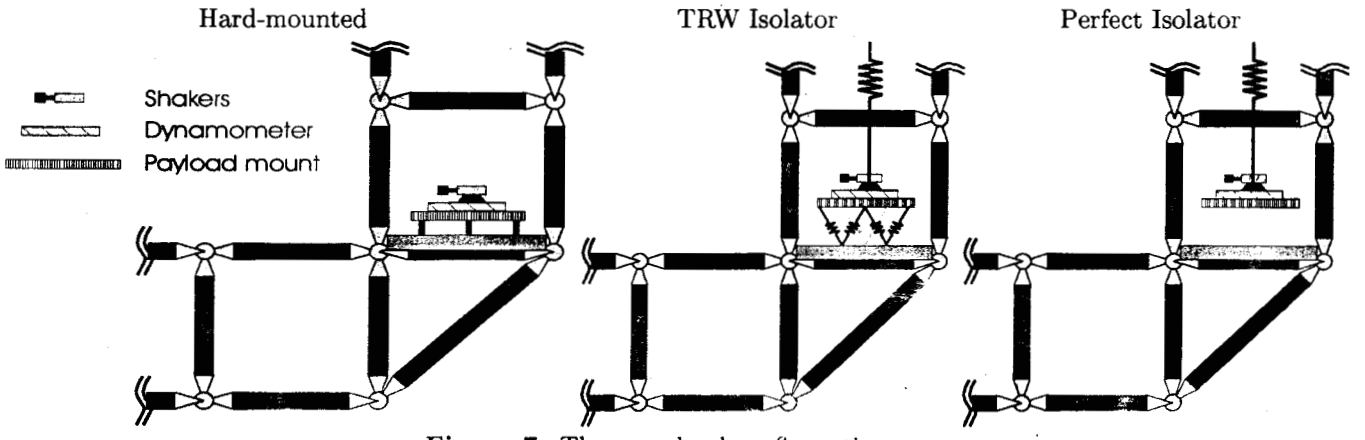

Figure 7. Three payload configurations.

plate of the testbed and the optics are passive. This represents a worse case scenario. Next is a case where the disturbance source is placed on top of a 6-axis vibration isolation system made by TRW. This is a more probably configuration for SIM, which corresponds to the tracking mode. Finally for the third configuration, we suspend the

*The justification of this metric is given by Neat end references therein.

disturbance source with a bungee cord from the same I-beam which suspends the testbed and closed the optics loop. This latter configuration no longer has a physical connection with the testbed. It therefor tests any electronic or acoustical coupling that may be present in the lab environment. The lack of coherence between our input disturbance and output centroid displacement indicates that there are no such flanking paths. This latter measurement is thus our measurement background noise.

6. RESULTS

A sample set of transfer functions are shown in Fig. 8. This is the response in the tip (x) direction on the camera

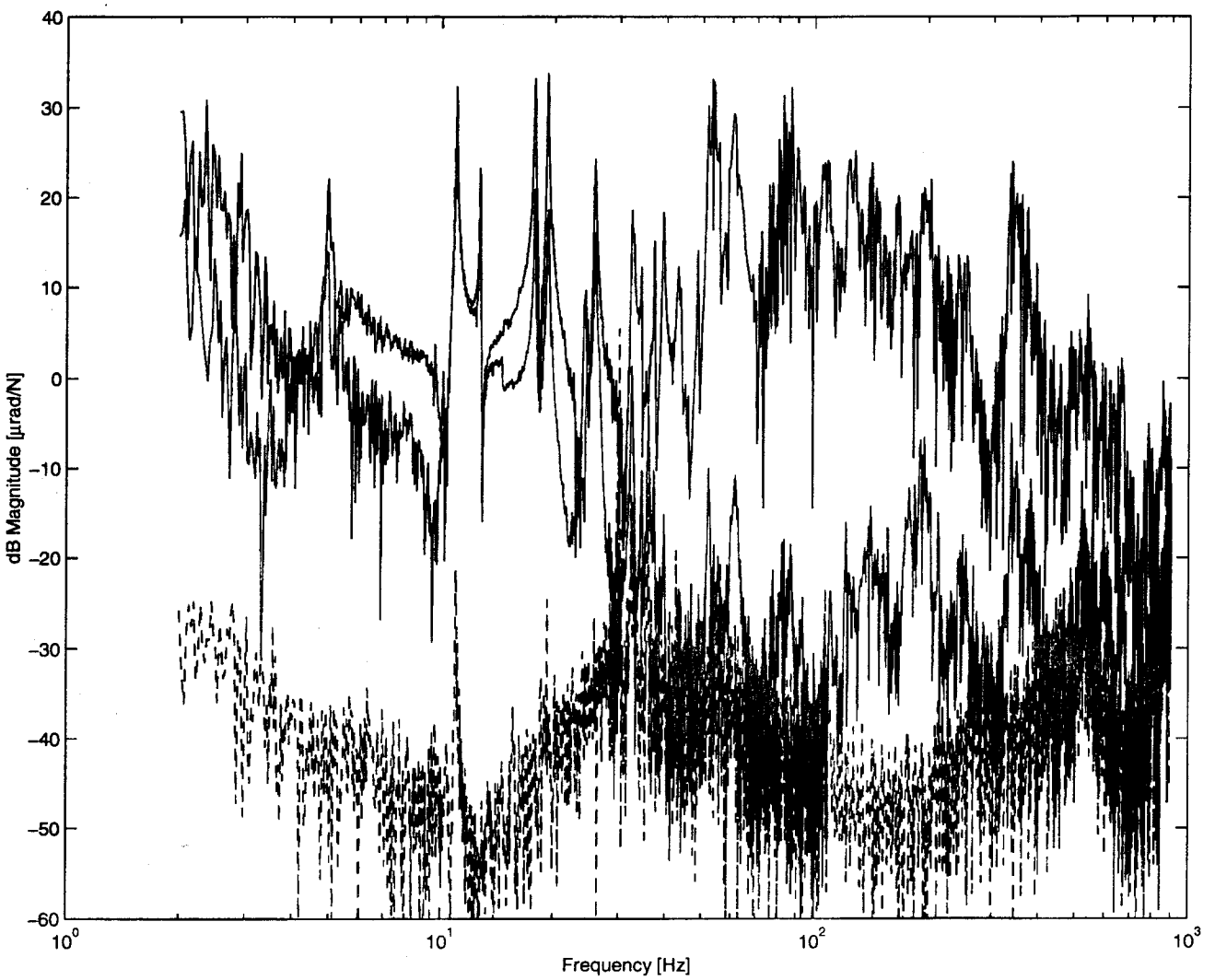

Figure 8. Comparison of the tilt wavefront tip (x) error while introducing a Y-force disturbance on the tested under different isolator and optics conditions.

when the testbed is disturbed along the y-direction. There are a total of twelve different sets of transfer functions : a tip (x) and tilt (y) for each of the three force and three torque disturbances. Note that for now, we have only measured the inboard (or right hand) arm transfer function. Each transfer function is sampled in three different frequency bands : from 2 to 14.5 Hz, from 14.5 to 100 Hz and from 100 to 900 Hz. The three bands are then spliced together. This is so that the driving voltage to the shakers can be adjusted across each band to produce adequate disturbance at higher frequencies without saturating the detector due to the lower frequency testbed modes.

Once a set of twelve transfer functions are measured for a particular configuration, we process the data to predict the on-orbit RMS jitter through the previously described method (Sec. 4). We multiply the reaction wheel spectrum

times the disturbance transfer functions for each RPM of the reaction wheels. This is done for all four reaction wheels along all six degrees of freedom. The total is summed together and yields the amount, in μradians, of combined tip/tilt motion of all the optics. Fig. 9 shows the predicted total tip/tilt jitter in μradians verses wheel speed for each of the test configurations. This is done for both the x and y directions. The results is then RSS over wheel

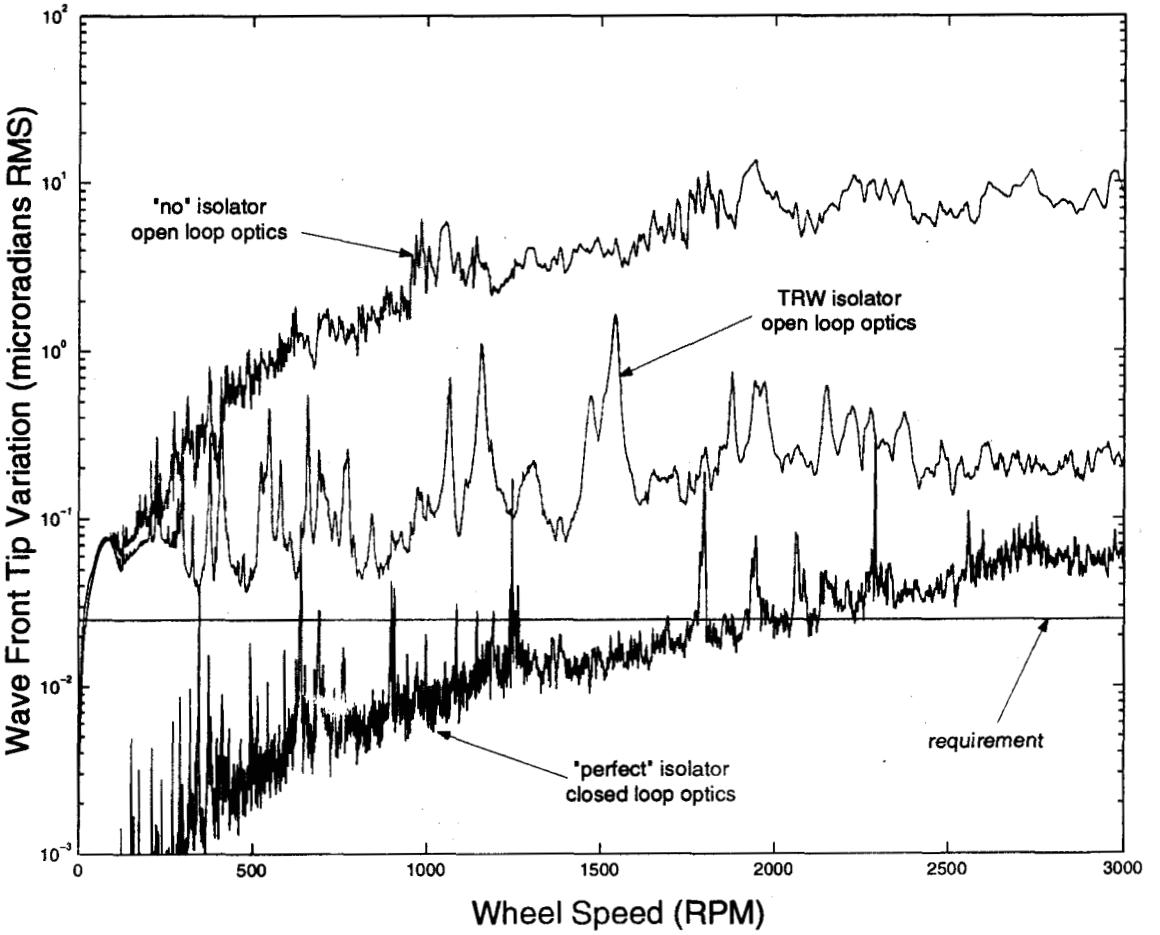

Figure 9. Predicted on-orbit wavefront tilt jitter verses reaction wheel speed for four configurations.

speed to form a predicted RMS jitter. The process is shown in Fig. 4. Table 2 shows the root sum squared (RSS) number of μradians for all configurations, where the RSS is taken over all RPM-s from 0 to 3000.

	Hard-mounted open loop	TRW isolator open loop	Perfect isolator closed loop
Inboard RMS Tip (x) jitter [nrad]	11430	518	67
Inboard RMS Tilt (y) jitter [nrad]	14250	871	62
Inboard RMS total jitter [nrad]	18270	1014	91
Total FSM jitter [nrad]	25840	1435	129

Table 2. Predicted tip/tilt jitter versus configuration.

7. DISCUSSION

Figure Fig. 9 susinctly summarizes the results of this study. For the most challenging astrometric pointing problem, the predictions suggest the jitter is above the requirement by a factor of 10 (compare the TRW isolator, open loop optics curve with the requirement). In addition, the predictions suggest that we have a sufficient noise floor to demonstrate the most challenging requirement except for the high reaction wheel speeds (compare the "perfect" isolator, closed loop optics curve with the requirement).

8. CONCLUSION

A method of predicting on-orbit residual jitter has been presented which is borrows from the already established on-orbit path length difference prediction algorithm. We have describe the beginning work on this and there are a number of improvements and further measurements that have been identified. These are : measure the outboard tip/tilt transfer functions and process the data in the same manner as was done here for the inboard side of the interferometer; further test different isolators, including elastomer cubes which have proven to work well for the OPD case; reduce the background noise in the MPI lab environment. Further possibilities are designing and building a method by which internal high frequency tip/tilt jitter can be measured independent from the star light. One final possibility for improvement, would be to use different, more quiet, reaction wheel assemblies for SIM. The first set of measurement are easily done, and will be performed on MPI. The later set are move involved and require SIM level trade studies before we can proceed.

ACKNOWLEDGMENTS

The work described in this paper was carried out at the Jet Propulsion Laboratory, California Institute of Technology, under contract wit the National Aeronautics and Space Administration.

REFERENCES

1. M. Shao and D. M. Wolf, "Orbiting stellar interferometer," in Reasenberg,[8] pp. 228–239.
2. R. A. Laskin and M. S. Martin, "Control/structure system design of a spaceborne optical interferometer," in *AAS/AIAA Astrodynamics Specialist Conference*, (Stowe, VT), Aug. 1989.
3. G. W. Neat, J. F. O'Brien, N. M. Nerheim, R. J. Calvet, H. Singh, and S. Shaklan, "Micro-precision interferometer testbed: First stabilized stellar fringes," in Reasenberg,[8] pp. 104–115.
4. G. W. Neat, A. Abramovici, J. W. Melody, R. J. Calvet, N. M. Nerheim, and J. F. O'Brien, "Control technology readiness for spaceborne optical interferometer missions," in *Proc. Space Microdynamics and Accurate Control Symposium*, (Toulouse, France), May 1997.
5. J. W. Melody and G. W. Neat, "Integrated modeling methodology validation using the micro-precision interferometer testbed," in *Proc. 35th IEEE Conference on Decision and Control*, vol. 4, pp. 4222–4227, (Kobe, Japan), Dec. 1996.
6. J. W. Melody, "Discrete-frequency and broadband reaction wheel disturbance models," Interoffice Memorandum 3411–95–200csi, JPL, June 1995.
7. A. Papoulis, *Probability, Random Variables, and Stochastic Processes*, McGraw-Hill, New York, 3rd ed., 1991.
8. R. D. Reasenberg, ed., vol. 2447 of *Proc. SPIE*, (Orlando, FA), Apr. 1995.

wit [redacted]